


 Cite this: *RSC Adv.*, 2018, **8**, 21968

 Received 21st April 2018  
 Accepted 5th June 2018

 DOI: 10.1039/c8ra03436b  
[rsc.li/rsc-advances](http://rsc.li/rsc-advances)

# Interlayer coupling and the phase transition mechanism of stacked MoS<sub>2</sub>/TaS<sub>2</sub> heterostructures discovered using temperature dependent Raman and photoluminescence spectroscopy

 Miao Chen,<sup>a</sup> Bin Zhou,<sup>a</sup> Fang Wang,<sup>a</sup> Liping Xu,<sup>a</sup> Kai Jiang,<sup>a</sup> Liyan Shang,<sup>\*a</sup>  
 Zhigao Hu<sup>ID</sup><sup>\*ab</sup> and Junhao Chu<sup>a</sup>

Ultrathin 1T (tetragonal)-TaS<sub>2</sub> and monolayer MoS<sub>2</sub> heterostructures were prepared to study their phase transition (PT) mechanisms and band structure modulation. The temperature dependency of photoluminescence (PL) and Raman spectra was utilized to study interlayer coupling and band structure. The PL results indicate that the band structure of MoS<sub>2</sub>/TaS<sub>2</sub> heterostructures undergoes a sharp change at 214 K. This is attributed to the PT of 1T-TaS<sub>2</sub> from a Mott insulator state to a metastable state. In addition, the temperature dependency of the MoS<sub>2</sub>/TaS<sub>2</sub> Raman spectra illustrates that the phonon vibration of the heterojunction is softened due to the effect of interlayer coupling. The present work could provide an avenue to create material systems with abundant functionalities and physical effects.

## 1 Introduction

2D heterojunctions play an important role in the rich clustering of electronic structures and their optical properties.<sup>1–3</sup> Recently, prominent progress in the field of heterojunctions has been made resulting in the development of high speed, performance and power devices.<sup>4–6</sup> Atom-thin heterojunctions as a new category of 2D semiconducting material are almost as thin, transparent and flexible as other 2D heterojunctions, with a rich array of new physical phenomena.<sup>2–5</sup> At this point, layered two-dimensional (2D) crystals such as transition metal dichalcogenides (TMDCs), graphene and hexagonal boron nitride have attracted noteworthy attention as different 2D materials that can be assembled vertically. Note that TMDCs are a broad family of compounds, which have layered two-dimensional (2D) crystal structures.<sup>7–11</sup> They have been recognized as promising materials due to their rich collection of electronic structures and optical properties.<sup>12–14</sup> In particular the noteworthy compound MoS<sub>2</sub>, taken as an example, has a direct band gap in single layer form while multilayers of the same material act as an indirect band gap semiconductor.<sup>15</sup> The transition allows for a much enhanced quantum yield of photoluminescence.<sup>16</sup> Another typical layered transition metal dichalcogenide (TMD),

1T (tetragonal)-TaS<sub>2</sub>, displays a sequence of unique structural and electronic phases. At low temperature and ambient pressure, the ground state is the commensurate charge density wave (CCDW) phase. As the temperature increases, it experiences a series of first-order phase transitions to a nearly commensurate (NC) CDW phase at 210 K, to an incommensurate (IC) CDW phase at 350 K, and finally to a metallic phase at 550 K. 1T-TaS<sub>2</sub> is an insulator in the C phase, arising from Fermi surface nesting.<sup>17–19</sup>

Single MoS<sub>2</sub> and 1T-TaS<sub>2</sub> materials have been widely researched. However, the interlayer coupling and band structures of MoS<sub>2</sub>/TaS<sub>2</sub> heterostructures were rarely studied using Raman and PL spectroscopy. In addition, it was reported that 1T-TaS<sub>2</sub> lacked the jump in resistivity that signals transition to the C phase for a few layers or a monolayer of material, or that the C phase was suppressed when the 1T-TaS<sub>2</sub> crystals became thinner than 10 nm,<sup>20,21</sup> but it was also reported that few-layer 1T-TaS<sub>2</sub> remained in the ground state. Therefore, it is still unknown whether ultrathin 1T-TaS<sub>2</sub> retains the CC to NC transition and produces an insulating state. Temperature change leads to lattice parameter changes and regulates the band structure, altering the optical properties of the heterojunctions. In addition, it is important to investigate whether the band gap structures of heterojunctions are tuned by the phase transition (PT) of 1T-TaS<sub>2</sub>. In this work, not only is few-layer 1T-TaS<sub>2</sub> studied using temperature dependent Raman spectra and the fitting results used to confirm the PT temperature (from CCDW to NCDW) as 214 K, but also the tuning of large-area 2D heterostructures is reported using chemical vapor deposition (CVD)-grown MoS<sub>2</sub> and ultrathin 1T-TaS<sub>2</sub> via mechanical

<sup>a</sup>Key Laboratory of Polar Materials and Devices (MOE), Technical Center for Multifunctional Magneto-Optical Spectroscopy (Shanghai), Department of Electronic Engineering, East China Normal University, Shanghai 200241, China. E-mail: [lyshang@ee.ecnu.edu.cn](mailto:lyshang@ee.ecnu.edu.cn); [zghu@ee.ecnu.edu.cn](mailto:zghu@ee.ecnu.edu.cn); Fax: +86-21-54345119; Tel: +86-21-54345150

<sup>b</sup>Collaborative Innovation Center of Extreme Optics, Shanxi University, Taiyuan, Shanxi 030006, China



exfoliation. In  $\text{MoS}_2$ – $\text{TaS}_2$  heterojunctions, interlayer coupling can be tuned externally with temperature variation. Our results also prove that the commensurate CDW remains in the ground state as the thickness of 1T- $\text{TaS}_2$  is decreased below 3 nm.

## 2 Experimental section

### 2.1 Construction of the heterojunctions

Ultrathin 1T- $\text{TaS}_2$  nanosheets were obtained *via* mechanical exfoliation onto  $\text{Si}/\text{SiO}_2$  (300 nm) from bulk 1T- $\text{TaS}_2$  crystals. They were kept in the vacuum chamber to minimize oxidation during the measurement. The bulk 1T- $\text{TaS}_2$  crystal was synthesized using chemical vapor transport (CVT) methods.<sup>22</sup> A  $\text{MoS}_2$  monolayer film was grown using a low-pressure CVD (at 30 Pa) technique for 5 minutes. First, the  $\text{SiO}_2/\text{Si}$  substrates were cleaned using piranha solution, then placed in the center of the quartz tube's heating zone and heated to 850 °C in an argon atmosphere to restrict further oxidation. Molybdenum sulfide ( $\text{MoCl}_5$ ) powder was loaded in front of the substrates, while sulfur powder was placed in the front of the quartz tube, which was heated to 200 °C. The stacked heterostructure was produced by transferring the monolayer  $\text{MoS}_2$  film onto the 2.9 nm 1T- $\text{TaS}_2$ . The as-grown monolayer film  $\text{MoS}_2$  was coated with a layer of the polymer polymethyl methacrylate (PMMA). The polymer acted as a carrier layer and it was helpful in transferring the  $\text{MoS}_2$  film. It was spin-coated on the CVD grown monolayer  $\text{MoS}_2/\text{SiO}_2/\text{Si}$  with a speed of 2000 rpm for 15 seconds. The PMMA/ $\text{MoS}_2/\text{SiO}_2/\text{Si}$  material was submerged into potassium hydroxide (KOH) solution. After the PMMA reacted with the KOH, the substrate was taken away. Then the PMMA/ $\text{MoS}_2$  was transferred into deionized water to remove any residual KOH solution.  $\text{TaS}_2/\text{SiO}_2/\text{Si}$  was put into the water from the side. The system was dried by simply sucking the water droplets away with a paper towel. The PMMA/ $\text{MoS}_2$  was positioned above the  $\text{TaS}_2/\text{SiO}_2/\text{Si}$  with tweezers. In order to combine the heterostructures better, the sample was baked at 90 °C for 30 min to remove water residue, and then at 120 °C for 30 min to spread the polymer to eliminate possible wrinkles. To dispel the PMMA, the transferred assembly was soaked in propanone for at least 2 hours and the propanone changed several times during this time.

### 2.2 Material characterization

Temperature dependent Raman scattering and photoluminescence (PL) measurements were carried out using a micro-Raman spectrometer with a Jobin-Yvon LabRAM HR 800 micro-Raman spectrometer and a THMSE 600 heating/cooling stage (Linkam Scientific Instruments) in the temperature range of 77 to 405 K with a resolution of 0.1 K. A laser with a wavelength of 532 nm was used as the excitation source. The laser beam was focused through a 50× microscope with a working distance of 18 mm. The laser power was limited to 10 mW in order to minimize the possibility of sample heating. An air-cooled charge coupled device (CCD) was used to collect the scattered signal dispersed on 1800 grooves per mm grating in the frequency range of 50–450  $\text{cm}^{-1}$ . All spectra were rectified by

the Bose–Einstein temperature factor to facilitate comparison and eliminate the contribution from the Bose–Einstein population factor. In order to study the variation trend of phonon modes, Raman spectra were fitted with independent damped harmonic oscillators.

### 2.3 Computational details

The density functional theory (DFT) calculations were executed with plane-wave pseudopotentials from the calculation method of quantum mechanics.<sup>23,24</sup> The Perdew–Burke–Ernzerhof generalized gradient approximation (GGA) for the exchange–correlation term was employed for structure optimization and band structure.<sup>25</sup> To acquire accurate results for multilayer structures, we incorporated the van der Waals interactions by adding a semi-empirical dispersion potential (D) to the conventional Kohn–Sham DFT energy. The structural parameters can be obtained from DFT-D which is in accordance with the experimental values. A well-converged Monkhorst–Pack *k*-point set ( $13 \times 13 \times 1$ ) was used for the calculation. A conjugate gradient scheme was employed to optimize the geometries until the forces on every atom were 0.005 eV  $\text{Å}^{-1}$ . Geometry optimization was determined using the Broyden–Fletcher–Goldfarb–Shanno (BFGS) minimization technique, with thresholds for the converged structure of energy change per atom smaller than  $10^{-5}$  eV. The vacuum thickness of a supercell is not smaller than 20 Å and spin–orbit coupling was not included.

## 3 Results and discussion

### 3.1 Morphology analysis and the temperature dependent Raman spectra of ultrathin 1T- $\text{TaS}_2$

High resolution transmission electron microscopy (HRTEM) was carried out at an accelerating voltage of 200 kV to gain detailed insight into the crystal structure of bulk 1T- $\text{TaS}_2$ . As shown in Fig. 1(a), the atomic image of bulk  $\text{TaS}_2$  exhibits the perfect triangular atomic arrangement. The lattice spacing of 2.94 Å is assigned to the (200) plane of 1T- $\text{TaS}_2$ . Fast Fourier transform (FFT) of the atomic image [Fig. 1(b)] further confirms the tetragonal crystal structure. In addition, the ultrathin 1T- $\text{TaS}_2$  topographies [Fig. 1(c)] and height [Fig. 1(d)] (2.76 nm) were investigated *via* atomic force microscopy (AFM, Dimension Icon, Bruker).

Fig. 2(a) shows the Raman spectra between 50 and 450  $\text{cm}^{-1}$  from a 2.76 nm flake for a series of temperatures during the heating process. All of the features of the Raman spectra at each temperature were in accordance with the results previously reported.<sup>26</sup> At low temperature, the phonons' vibration is intensified and the modes near about 70  $\text{cm}^{-1}$ , 86  $\text{cm}^{-1}$  and 105  $\text{cm}^{-1}$  split into explicit peaks. Additional peaks, which appeared in the commensurate CDW state, are due to the folding of the  $\Gamma$ -point modes from the original non-zero wave vector points by the formation of the  $\sqrt{13}a_0 \times \sqrt{13}a_0$  superlattice.<sup>27,28</sup> At high temperature, some modes in the range of 50–450  $\text{cm}^{-1}$  become weaker gradually and disappear finally, manifesting in the reduction of structural distortion. The modes near 305  $\text{cm}^{-1}$  exhibit a slight redshift with increasing



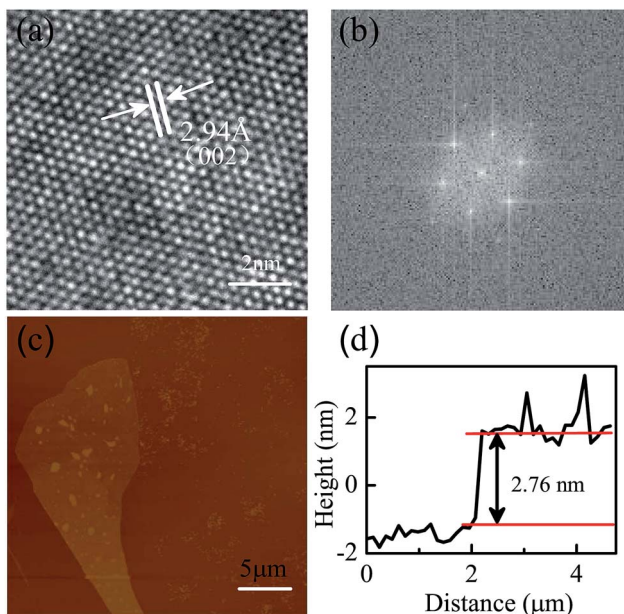


Fig. 1 (a) A high resolution transmission electron microscopy (HRTEM) image of bulk 1T-TaS<sub>2</sub>. Panel (b) shows the Fast Fourier transform (FFT) of the atomic image. The (c) AFM image and (d) height profile of few-layer 1T-TaS<sub>2</sub>.

temperature, which can be attributed to the thermal expansion of the lattice and anharmonic phonon-phonon interactions. The modes with a frequency below 140 cm<sup>-1</sup> come from the acoustic phonon branches where mainly tantalum atoms move. Those above 220 cm<sup>-1</sup> arise from the optical phonon branches where mainly selenium atoms move.<sup>27,28</sup> In order to determine the accurate temperature at which the PT (from CCDW to NCDW) takes place, some temperature dependent phonon frequencies are extracted and shown in Fig. 2(b) and (c). There are clear changes in the temperature range of 210–230 K. For example, it can be seen that part of the phonon modes disappears or merges with other modes at the transition from the commensurate to the nearly commensurate phase. The soft A<sub>g</sub>-modes located at about 81 cm<sup>-1</sup> and 114 cm<sup>-1</sup> are particularly noteworthy and undergo severe variations in linewidth and energy, and are marked with stars and triangles in Fig. 2(b).

### 3.2 Morphology characteristics and interlayer coupling of the MoS<sub>2</sub>/TaS<sub>2</sub> heterostructure

The vertically stacked heterostructure has been investigated using a Raman scattering technique. An optical image of the MoS<sub>2</sub>/TaS<sub>2</sub> heterostructure is shown in Fig. 3(e). It indicates that the MoS<sub>2</sub>/TaS<sub>2</sub> heterostructure has been stacked successfully. The bottom 1T-TaS<sub>2</sub> topographies and height (2.9 nm) are displayed in Fig. 3(f). The optical images and topographies of the top MoS<sub>2</sub> film are demonstrated in Fig. 3(g) and (h). They indicate that the monolayer MoS<sub>2</sub> film was successfully prepared. Fig. 3(a) and (b) show the Raman shift for the MoS<sub>2</sub>/TaS<sub>2</sub> heterostructure and monolayer MoS<sub>2</sub>, respectively, as a function of temperature. In Fig. 3(b), a downward shift of the MoS<sub>2</sub> Raman modes with increasing temperature is shown. This

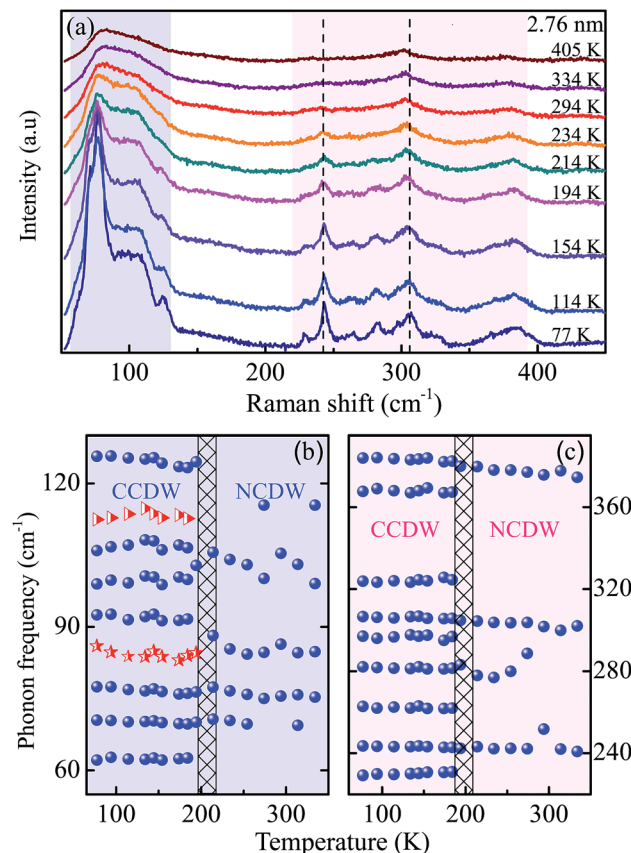
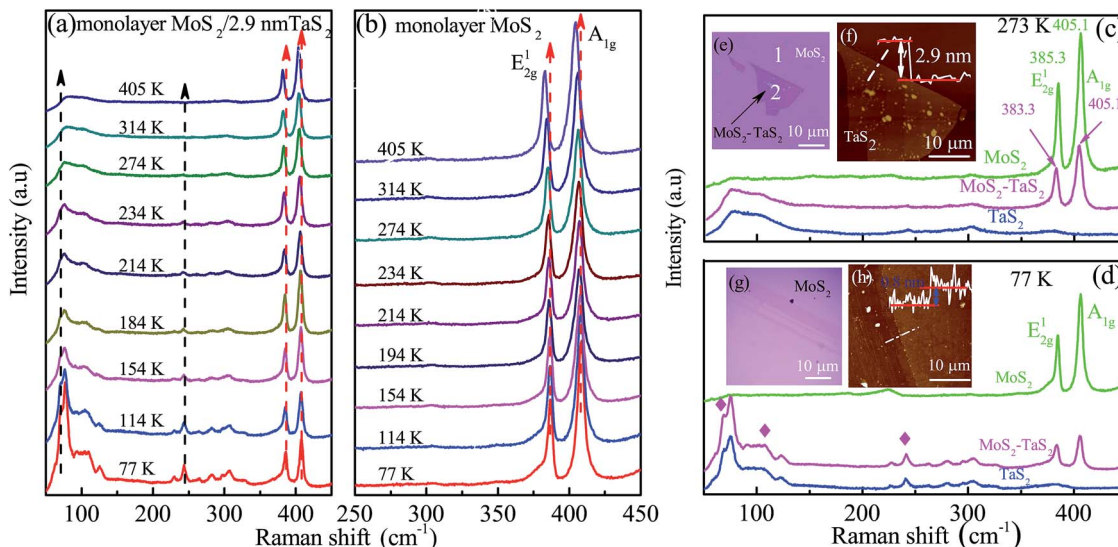


Fig. 2 (a) Raman spectra of a 2.76 nm-thick flake at different temperatures during the heating process. Temperature dependence of the phonon frequency from the 2.76 nm-thick flake from (b) the low frequency range of 55–130 cm<sup>-1</sup> and (c) the high frequency range of 220–390 cm<sup>-1</sup>. The phase transition (CC–NC) temperature is marked by a dashed line in (b) and (c).

behavior is due to the influence of the anharmonicity and the effect of thermal expansion or volume contribution. As shown in Fig. 3(a), it was found that the E<sub>2g</sub><sup>1</sup> and A<sub>1g</sub> phonon modes from MoS<sub>2</sub> are suppressed in the heterostructures, which can be attributed to the softening of the phonon mode by the interlayer coupling of MoS<sub>2</sub>/TaS<sub>2</sub>.

To further explore the effect of interlayer coupling on the heterojunction, we compared the phonon vibration spectrum of MoS<sub>2</sub>, MoS<sub>2</sub>/TaS<sub>2</sub> and TaS<sub>2</sub> at the same temperature. As shown in Fig. 3(c), E<sub>2g</sub><sup>1</sup> and A<sub>1g</sub> phonon modes are located at about 385.3 cm<sup>-1</sup> and 405.1 cm<sup>-1</sup> for monolayer MoS<sub>2</sub> at 273 K. The frequency difference between the E<sub>2g</sub><sup>1</sup> and A<sub>1g</sub> phonon modes is 19.8 cm<sup>-1</sup> for the monolayer MoS<sub>2</sub> in MoS<sub>2</sub>/TaS<sub>2</sub>.<sup>29</sup> The Raman mode E<sub>2g</sub><sup>1</sup> significantly stiffened by 2 cm<sup>-1</sup> and the A<sub>1g</sub> mode was unchanged in the multilayer MoS<sub>2</sub>/TaS<sub>2</sub> heterostructure, as compared with those in the isolated MoS<sub>2</sub> monolayer from Fig. 3(c). This was due to the E<sub>2g</sub><sup>1</sup> and A<sub>1g</sub> modes being sensitive to strain<sup>30</sup> and the doping level<sup>31,32</sup> in MoS<sub>2</sub>, respectively. Therefore, the shifted E<sub>2g</sub><sup>1</sup> mode and the unchanged A<sub>1g</sub> mode of MoS<sub>2</sub> imply that the strain relaxes differently for MoS<sub>2</sub>/TaS<sub>2</sub> compared to that of MoS<sub>2</sub>/SiO<sub>2</sub>, and such a result indicates strong interlayer coupling between TaS<sub>2</sub> and MoS<sub>2</sub>. The Raman



**Fig. 3** Raman spectra of the  $\text{MoS}_2/\text{TaS}_2$  heterostructure (a) and monolayer  $\text{MoS}_2$  (b) at different temperatures during the heating process. Raman spectra of the  $\text{MoS}_2$ ,  $\text{TaS}_2$  and  $\text{MoS}_2\text{-TaS}_2$  heterostructures at 77 K (c) and 273 K (d), respectively. (e) An optical microscope image of the  $\text{MoS}_2\text{-TaS}_2$  heterostructure. (f) The AFM image and height (2.9 nm) profile of few-layer 1T-TaS<sub>2</sub>. (g) An optical microscope image of monolayer  $\text{MoS}_2$ . (h) The AFM image and height (0.8 nm) profile of monolayer  $\text{MoS}_2$ .

spectra of the  $\text{MoS}_2\text{-TaS}_2$  heterostructure seem to be a simple superposition of the 2.9 nm  $\text{TaS}_2$  and monolayer  $\text{MoS}_2$ . At 77 K, these phonon modes (marked with a diamond symbol) split into several well-defined peaks and the mode at  $384 \text{ cm}^{-1}$  of  $\text{TaS}_2$  overlaps the  $\text{MoS}_2$   $E_{2g}^1$  Raman modes for the  $\text{MoS}_2\text{-TaS}_2$  heterostructure.

### 3.3 The band structures of monolayer $\text{MoS}_2$ , few-layer $\text{TaS}_2$ and $\text{MoS}_2\text{/TaS}_2$ heterostructures

Before the PL spectra of the heterostructure were obtained, we calculated the band structure of monolayer  $\text{MoS}_2$ , 4 layered 1T-TaS<sub>2</sub> and their heterojunctions. As shown in Fig. 4(a), the theoretical results show that the bandgap of the  $\text{MoS}_2$

monolayer is about 1.9 eV. The valance band maximum (VBM) and conduction band minimum (CBM) are located at the  $K$  point in the Brillouin zone, which is due to the Mo d-orbitals. The Mo atoms are located in the middle of the S-Mo-S layer sandwiches and are unaffected by interlayer coupling. For the 4 layered 1T-TaS<sub>2</sub>, the band structure is similar to that of the pristine sample.<sup>33</sup> There is a gap of about 0.8 eV below the band crossing Fermi energy ( $E_f$ ) as shown in Fig. 4(b) and one band crosses the  $E_f$ , forming a 2D electron pocket around the  $M$  point. In addition, it can be seen that the band diagram of the heterojunction is a combination of the monolayer layer  $\text{MoS}_2$  and few-layer  $\text{TaS}_2$ , as shown in Fig. 4(c).

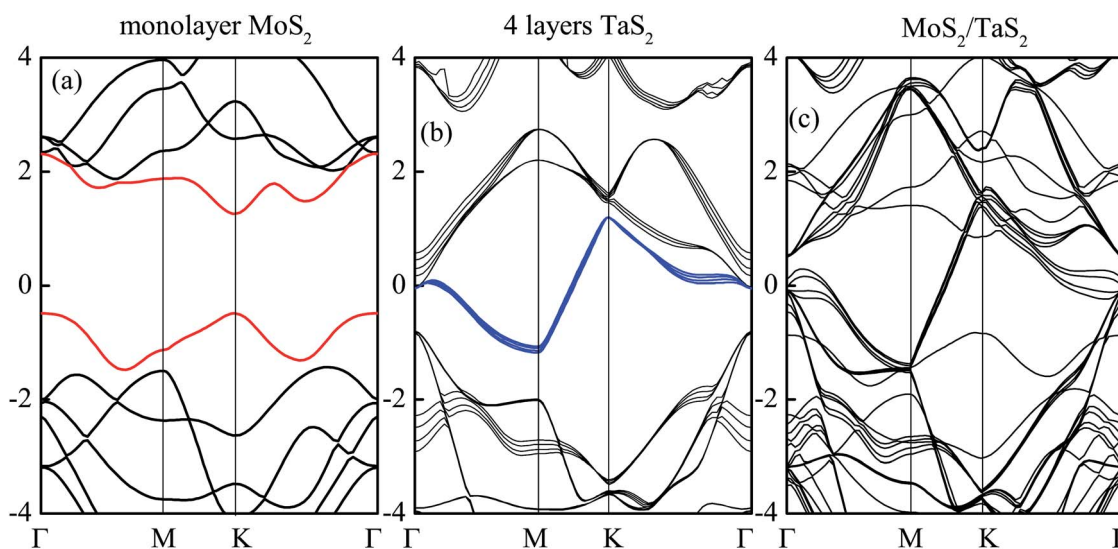


**Fig. 4** The band structures for (a) monolayer  $\text{MoS}_2$ , (b) few-layer  $\text{TaS}_2$  and (c)  $\text{MoS}_2\text{-TaS}_2$  heterostructures.

### 3.4 The transition mechanism of the MoS<sub>2</sub>/TaS<sub>2</sub> heterostructure

Interlayer interaction is expected to be exponentially sensitive to the interlayer spacing according to tight-binding theory or the quantum tunneling model. To investigate interlayer coupling with different interlayer distances, a variable-temperature tuning process was performed for the monolayer MoS<sub>2</sub> and MoS<sub>2</sub>/TaS<sub>2</sub> heterostructures. The PL spectra at 77 K (Fig. 5) collected from the monolayer MoS<sub>2</sub> region show a strong peak at a wavelength of about 1.89 eV, which corresponds to the direct excitonic transition energy in monolayer MoS<sub>2</sub>. However, for the MoS<sub>2</sub>/TaS<sub>2</sub> heterostructure (region 2, Fig. 3(e)), two peaks are observed at about 1.86 and 1.67 eV for 77 K. The peak located at 1.86 eV from MoS<sub>2</sub> is marked P<sub>MoS<sub>2</sub></sub>. Another peak located at 1.67 eV was attributed to the direct excitonic transition energies in the top MoS<sub>2</sub> and bottom ultrathin TaS<sub>2</sub> materials at 77 K. It is marked P<sub>hetero</sub>. In addition, the MoS<sub>2</sub>/TaS<sub>2</sub> heterostructure forms a type II band alignment.<sup>34,35</sup> In the type II heterojunction, the CBM and VBM reside in two separate materials. As shown in the inset schematic diagram of Fig. 6, photoexcited electrons and holes will relax to the conduction band edge of TaS<sub>2</sub> when the temperature is varied from 77 K to 214 K. A P<sub>hetero</sub> peak at about 1.67 eV is observed at 77 K, 114 K and 194 K as shown in Fig. 5, interestingly lying at a lower energy than the peak for the single layers of MoS<sub>2</sub>. This suggests that the type II band alignment in the MoS<sub>2</sub>/TaS<sub>2</sub> facilitates the photoexcited electron–hole separation and leads to an enhanced photoswitching performance, as compared to that in MoS<sub>2</sub> and TaS<sub>2</sub>.<sup>36</sup> However, the P<sub>hetero</sub> peak disappears in the MoS<sub>2</sub>/TaS<sub>2</sub> heterostructure when the temperature is beyond 214 K, which is because of the appearance of domain walls. 1T-TaS<sub>2</sub> is in the nearly commensurate CDW phase. It also has long

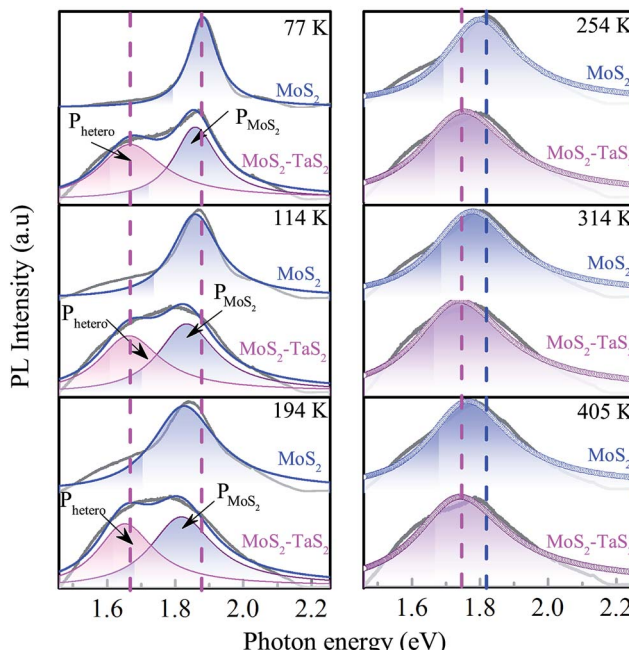


Fig. 5 PL spectra of MoS<sub>2</sub> and MoS<sub>2</sub>/TaS<sub>2</sub> heterostructures at different temperatures during the heating process.

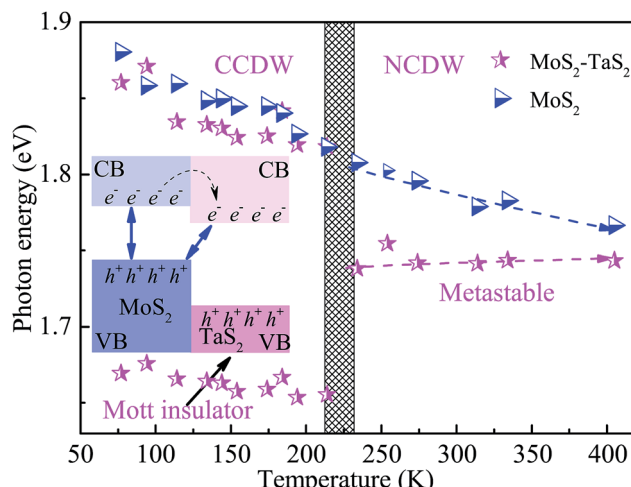


Fig. 6 PL peak position of the MoS<sub>2</sub> and MoS<sub>2</sub>/TaS<sub>2</sub> heterostructures. The inset shows the schematic of the band alignment for the MoS<sub>2</sub>-TaS<sub>2</sub> heterostructure at low temperature.

been assumed that electron correlations open up a Mott-Hubbard gap in the C phase.<sup>37</sup> In addition, electron–electron interactions, electron–phonon coupling, interlayer interactions and disorder could play an important role in this observation. As shown in Fig. 5 (254 K, 314 K and 405 K), the energy band spectra of the MoS<sub>2</sub>/TaS<sub>2</sub> heterostructure is very similar to those of the monolayer MoS<sub>2</sub>. There is a difference of 14 meV between the monolayer MoS<sub>2</sub> and MoS<sub>2</sub>/TaS<sub>2</sub> heterostructure at 254 K, which is owing to the influences of a TaS<sub>2</sub> atomic layer for monolayer MoS<sub>2</sub>. These results show that the ultrathin 1T-TaS<sub>2</sub> exhibits abrupt and reversible changes in the lattice structure, which are attractive for device applications.

With the purpose of further studying the phase transition mechanism of the MoS<sub>2</sub>/TaS<sub>2</sub> heterojunction, we respectively fit the PL spectra of MoS<sub>2</sub> and the MoS<sub>2</sub>/TaS<sub>2</sub> heterojunction to compare their characteristics, as shown in Fig. 6. The redshift of the monolayer from the MoS<sub>2</sub> PL peak with an increase in temperature indicates a reduction in the MoS<sub>2</sub> energy band gap, which is the energy of the lowest allowed exciton state. In addition, most of the energy gaps of the heterojunction are less than those from MoS<sub>2</sub> as shown in Fig. 6. This indicates that the heterojunction regulates the band structure of MoS<sub>2</sub>, reducing the band gap and increasing the conductivity. The modified Varshni relationship of the band-gap temperature dependence is fitted using the following formula:<sup>38,39</sup>

$$E(T) = E_0 - S \langle \hbar \omega \rangle \left[ \coth \frac{\langle \hbar \omega \rangle}{2k_B T} - 1 \right]. \quad (1)$$

where E<sub>0</sub> represents the emission energy at T = 0 K, S is the parameter which describes the coupling strength of an exciton-phonon,  $\langle \hbar \omega \rangle$  is an average phonon energy, and k<sub>B</sub> and  $\hbar$  are the Boltzmann and Planck constants, respectively. Another phenomena that is evident is that the two PL fitting peaks at low temperature combine into one peak at 214 K. This suggests that the C phase disappears gradually and the NC phase emerges.

## 4 Conclusions

In summary, the interlayer coupling and phase transition mechanism were studied by variable-temperature spectral experiment. The results of Raman spectroscopy indicate that interlayer coupling causes phonon softening of MoS<sub>2</sub>/TaS<sub>2</sub> heterostructures. It was also found that the MoS<sub>2</sub>/TaS<sub>2</sub> heterostructure forms a type II band alignment. A P<sub>hetero</sub> peak appears when the TaS<sub>2</sub> is located in the C phase. Furthermore, this phenomenon also confirms that commensurate CDW remains in the ground state as the 1T-TaS<sub>2</sub> is thinned to 3 nm. These results distinguish the significance of band offsets between different TMDs in tuning the light emission and band structure. It is believed that the analysis method described in our work could be helpful in exploring the interlayer coupling of other similar TMDs.

## Conflicts of interest

There are no conflicts to declare.

## Acknowledgements

This work was financially supported by the National Key Research and Development Program of China (Grant No. 2017YFA0303403), Natural Science Foundation of China (Grant No. 61674057 and 61227902), Projects of Science and Technology Commission of Shanghai Municipality (Grant No. 18JC1412400, 18YF1407200, 18YF1407000 and 15JC1401600), and the Program for Professor of Special Appointment (Eastern Scholar) at Shanghai Institutions of Higher Learning and the Fundamental Research Funds for the Central Universities.

## References

- 1 K. F. Mak, C. G. g. Lee, J. Hone, J. Shan and T. F. Heinz, *Phys. Rev. Lett.*, 2010, **105**, 136805.
- 2 Q. W. Wang, K. Kalantar-Zadeh, K. Andras, J. N. Coleman and M. S. Strano, *Nat. Nanotechnol.*, 2012, **7**, 699.
- 3 T. Yu and M. W. Wu, *Phys. Rev. B*, 2016, **93**, 045414.
- 4 H. Kroemer, *Proc. IEEE*, 1982, **70**, 13.
- 5 B.-S. Kim, D. C. J. Neo, B. Hou, J. Park, Y. Cho, N. Zhang, J. Hong, S. Pak, S. Lee, J. Sohn, H. E. Assender, A. A. R. Watt, S. Cha and J. Kim, *ACS Appl. Mater. Interfaces*, 2016, **8**, 13902.
- 6 X. Hong, J. Kim, S.-F. Shi, Y. Zhang, C. Jin, Y. Sun, S. Tongay, J. Wu, Y. Zhang and F. Wang, *Nat. Nanotechnol.*, 2014, **9**, 682.
- 7 A. Aruchamy and M. K. Agarwal, *Photoelectrochemistry and Photovoltaics of Layered Semiconductors*, 1992, vol. 14, p. 1319.
- 8 S. J. Yun, G. H. Han, H. Kim, D. L. Duong, B. G. Shin, J. Zhao, Q. A. Wu, J. Lee, S. M. Lee and Y. H. Lee, *Nat. Commun.*, 2017, **8**, 2163.
- 9 Z. H. Ji, H. Hong, J. Zhang, Q. Zhang, W. Huang, T. Cao, R. X. Qiao, C. Liu, J. Liang and C. H. Jin, *ACS Nano*, 2017, **11**, 12020–12026.
- 10 D. Kozawa, A. Carvalho, I. Verzhbitskiy, F. Giustiniano, Y. Miyauchi, S. Mouri, A. H. Castro, K. Matusda and G. Eda, *Nano Lett.*, 2016, **16**, 4087–4093.
- 11 C. H. Ho, W. H. Chen, K. K. Tiong, K. Y. Lee, A. Gloter, A. Zobell, O. Stephan and L. H. G. Tizel, *ACS Nano*, 2017, **11**, 11162–11168.
- 12 K. Geim and I. V. Grigorieva, *Nature*, 2013, **419**, 499.
- 13 L. G. Ma, Y. Cun, Y. J. Yu, X. F. Lu, X. H. Niu, S. Kim, D. L. Feng, D. Tománek, Y. W. Son, X. H. Chen and Y. B. Zhang, *Nat. Commun.*, 2016, **7**, 10956.
- 14 M. J. Hollander, Y. Liu, W. J. Lu, L. J. Li, Y. P. Sun, J. A. Robinson and S. Datta, *Nano Lett.*, 2015, **15**, 1861–1866.
- 15 L. Wang and M. W. Wu, *Phys. Rev. B: Condens. Matter Mater. Phys.*, 2014, **89**, 205401.
- 16 A. M. Yan, J. Velasco, S. Kahn, K. Watanabe, T. Taniguchi, F. Wang, M. F. Crommie and A. Zettl, *Nano Lett.*, 2015, **15**, 6324.
- 17 R. He, J. C. Okamoto, Z. P. Ye, G. h. Ye, H. D. Anderson, X. Dai, X. X. Wu, J. P. Hu, Y. Liu, W. J. Lu, Y. P. Sun, A. N. Pasupathy and A. W. Tsien, *Phys. Rev. B*, 2018, **94**, 201108.
- 18 B. Sipos, A. F. Kusmartseva, A. Akrap, H. Berger, L. Forro and E. Tutis, *Nat. Mater.*, 2008, **8**, 960.
- 19 A. H. Thompson, F. R. Gamble and J. F. Revelli, *Solid State Commun.*, 1971, **9**, 981.
- 20 Y. J. Yu, F. Y. Yang, X. F. Lu, Y. J. Yan, Y. H. Cho, L. Ma, X. H. Niu, S. Kim, Y. W. Son, D. L. Feng, S. Y. Li, S. W. Cheong, X. H. Chen, Y. B. Zhang, A. L. Mayer, J. R. Guest and S. W. Hla, *Nat. Nanotechnol.*, 2015, **10**, 270.
- 21 J. R. Guest and S. W. Hla, *Physics arXiv:1506.04102*, 2015.
- 22 Y. Liu, R. Ang, W. Lu, W. Song, L. Li and Y. Sun, *Appl. Phys. Lett.*, 2013, **102**, 192602.
- 23 P. Hohenberg and W. Kohn, *Phys. Rev.*, 1964, **136**, B864–B871.
- 24 D. Vanderbilt, *Phys. Rev. B: Condens. Matter Mater. Phys.*, 1990, **41**, 7892.
- 25 J. P. Perdew and Y. Wang, *Phys. Rev. B: Condens. Matter Mater. Phys.*, 1992, **45**, 13244–13249.
- 26 O. R. Albertini, R. Zhao, R. L. McCann, S. Feng, M. Terrones, J. K. Freericks, J. A. Robinson and A. Y. Liu, *Phys. Rev. B*, 2016, **93**, 214109.
- 27 S. Sugar, K. Murase, S. Uchida and S. Tanaka, *Physica B*, 1981, **105**, 405.
- 28 B. Dardel, M. Grioni, D. Malterre, P. Weibel and Y. Baer, *Phys. Rev. B: Condens. Matter Mater. Phys.*, 1992, **45**, 3.
- 29 X. Luo, Y. Y. Zhao, J. Zhang, M. L. Toh, C. Kloc, Q. H. Xiong and S. Y. Quek, *Phys. Rev. B: Condens. Matter Mater. Phys.*, 2013, **88**, 195313.
- 30 C. Rice, R. J. Young, R. Zan, U. Bangert, D. Wolverson, T. Georgiou, R. Jalil and K. S. Novoselov, *Phys. Rev. B: Condens. Matter Mater. Phys.*, 2013, **87**, 5.
- 31 B. Chakraborty, A. Bera, D. V. S. Muthu, S. Bhowmick, U. V. Waghmare and A. K. Sood, *Phys. Rev. B: Condens. Matter Mater. Phys.*, 2012, **85**, 4.
- 32 M. Buscema, G. A. Steele, H. S. J. van der Zant and A. Castellanos-Gomez, *Nano Res.*, 2014, **7**, 561.



33 J. A. Wilson, F. J. Di Salvo and S. Mahajan, *Adv. Phys.*, 1975, **24**, 117.

34 H. Terrones, F. López-Urias and M. Terrones, *Sci. Rep.*, 2013, **3**, 1549.

35 K. Jun, T. Sefaattin, J. Zhou, J. B. Li and J. Q. Wu, *Appl. Phys. Lett.*, 2013, **102**, 012111.

36 N. Huo, J. Yang, L. Huang, Z. Wei and S. Li, *Small*, 2015, **11**, 5430.

37 P. Fazekas and E. Tosatti, *Physica B*, 1980, **99**, 183.

38 H. Y. Fan, *Phys. Status Solidi*, 1967, **34**, 149.

39 A. A. Mitioglu, P. Plochocka, J. N. Jadcak, W. Escoffier, G. L. J. A. Rikken, L. Kulyuk and D. K. Maude, *Phys. Rev. B: Condens. Matter Mater. Phys.*, 2013, **88**, 245403.

